In: AIAA SCITECH 2026 Forum, 12-16 January 2026,
Orlando, Florida, USA, Article number 2026-2569
DOI: 10.2514/6.2026-2569

Unsteady Swirl Distortion Characterization in a Coupled Fan-Intake System in Crosswind Conditions Using Stereoscopic Particle Image Velocimetry

Tommaso Piovesan[1], Pavlos K. Zachos[2] and David G. MacManus[3]
Faculty of Engineering and Applied Sciences, Cranfield University, Cranfield, UK

Swirl distortion is one of the key factors influencing the aerodynamic performance of coupled intake–fan systems. This study presents a detailed analysis of Stereoscopic Particle Image Velocimetry (S-PIV) data acquired on a circular plane within an aero-engine intake operating under crosswind conditions, including a ground plane and a co-rotating ground vortex ingested ahead of a rotating fan. Two flow conditions were examined: one exhibiting diffusion-driven separation at low fan speed and Mass Flow Capture Ratio (MFCR), and another with attached flow at higher fan speed and MFCR, both at constant crosswind velocity. This work demonstrates the effective implementation of PIV measurement techniques to a coupled fan–intake system in an industrial setting, achieving unprecedented flow-field resolution and data fidelity. Swirl distortion descriptors obtained from experimental data are used to produce Extreme Value Theory (EVT)-based forecasts of peak swirl intensity, which is the novelty of the work. Key contribution includes the identification of notably different swirl distortion characteristics between attached and separated intake flow conditions. Fan-face swirl distortion was found to be significantly more severe in the separated case, with time-averaged and peak swirl intensities up to three and four times higher, respectively, than in the attached case. The analysis at a radial position near the fan tip showed that peak swirl distortion can differ substantially from global, area-averaged metrics. These high distortion levels, particularly near the fan tip, indicate a potentially significant reduction in rotor incidence angle and, consequently, a loss in fan performance. The impact of this work is the establishment of an experimental and analytical framework that advances the understanding and quantification of swirl distortion in coupled fan-intake systems, offering a basis for improved industry standards, shorter testing durations, and more accurate prediction of extreme distortion levels.

I. Nomenclature

$\dot{m}$	=	intake mass flow rate, kg/s
A_{HL}	=	highlight area, m^2
AIP	=	Aerodynamic Interface Plane
D_{HL}	=	highlight diameter, m
D	=	intake inner diameter, m
EVT	=	Extreme Value Theory
FPR	=	Fan Pressure Ratio
h	=	vertical distance from lowest point of the highlight plane to ground plane, m
L	=	intake length, m

[1] Research Fellow, Centre for Propulsion and Thermal Power Engineering.
[2] Reader in Propulsion Aerodynamics, Centre for Propulsion and Thermal Power Engineering, AIAA Senior Member.
[3] Professor in Propulsion Aerodynamics, Centre for Propulsion and Thermal Power Engineering, AIAA Member.

Published by AIAA. This is the Author Accepted Manuscript issued with: Creative Commons Attribution License (CC:BY 4.0).
The final published version (version of record) is available online at DOI:10.2514/6.2026-2569. Please refer to any applicable publisher terms of use.

$MFCR$	=	Mass Flow Capture Ratio
PDF^*	=	normalized Probability Density Function
R_{AIP}	=	AIP radius, m
RPM	=	rotations per minute, RPM
SD	=	Swirl Directivity
SI	=	Swirl Intensity, deg
U_b	=	upper bound, deg
V_∞	=	freestream velocity, m/s
α	=	swirl angle, degrees
ρ_∞	=	freestream density, kg/m^3

II. Introduction

Reducing fuel consumption and environmental impact are key objectives in the design of future civil aviation turbofan engines [1]-[3]. One promising area of improvement is engine installation, where new intake designs, shorter and slimmer than conventional ones, are being developed to reduce the overall weight and drag for larger fan-diameter engines [4][5], thereby enhancing overall performance. However, these compact intake configurations have less internal diffusion capability and interact more directly with the fan rotor compared to conventional designs [6][7]. This can lead to complex flow distortions that may affect fan-intake compatibility, especially under off-design conditions such as crosswinds. Crosswind and ground proximity introduce additional challenges in the aerodynamic design process and performance assessment of propulsion systems coupled with short intakes. A ground vortex may form due to flow interaction with the runway, while flow separation can occur on the windward side of the intake. Together, they may adversely impact the aerodynamic and mechanical performance of the propulsion system. A detailed understanding of intake flow characteristics under off-design conditions is therefore critical for designing efficient, distortion-tolerant intake-fan systems. Many studies have examined intake flows under crosswind conditions using both experiments and numerical simulations. Earlier research investigated the formation mechanisms of ground vortices [8]-[10] and the correlation between their characteristics and the intake operating conditions and geometry [11]-[14]. Windward lip separation caused by crosswinds has also been extensively studied, both experimentally [15][16] and numerically [17]-[20]. More recent work has focused on the unsteady behaviour of ground vortices, quantifying how their strength and size change in front of and beneath the intake [21]-[29]. Other studies have analysed the coupled aerodynamics of intake-fan rotor systems in crosswind conditions, primarily through numerical simulations, focusing mainly on total pressure distortion caused by intake flow separation [30][31] and on the fan forced response to the ground vortex [32][33].

From an experimental standpoint, current industry standards rely on a limited number of intrusive pressure sensors, typically arranged on rakes at the Aerodynamic Interface Plane (AIP) between the intake and the engine, to characterize intake flow fields [34], with a primary focus on total pressure distortion. However, the intrusive nature of such instrumentation and the associated blockage effects limit the number of sensors that can be employed, preventing full capture of the spatial complexity of the flow [35]. As a result, important flow features may be missed, limiting the understanding and quantification of the unsteady distortion within the intake. In particular, swirl distortion arising from flow separation and vortex ingestion at the AIP has not been characterized in sufficient detail, primarily due to the lack of high-resolution measurements in coupled intake-fan systems. Recent research has demonstrated the feasibility of applying non-intrusive optical methods in wind tunnel environments [36][37] and industrial engine tests [38] to measure unsteady velocity fields across a plane within intakes. Using Stereoscopic Particle Image Velocimetry (S-PIV), these studies achieved a spatial resolution approximately two orders of magnitude higher than those provided by conventional methods [35].

This work presents a detailed analysis of the unsteady flow distortion at the Aerodynamic Interface Plane (AIP) in a coupled intake-fan system operating under crosswind conditions. High-resolution, time-resolved velocity fields were obtained using Stereoscopic Particle Image Velocimetry (S-PIV) on a circular plane upstream of a rotating fan in an experimental set-up that also included a ground plane. For the first time in this context, swirl distortion metrics were evaluated to quantify the levels of swirl distortion in front of the fan and Extreme Value Theory (EVT) was applied to predict peak distortion levels beyond the measurement duration. The novelty of this work lies in demonstrating fully non-intrusive, high-resolution measurements of unsteady swirl distortion within a representative intake-fan system under crosswind conditions. This study shows a successful application of Particle Image Velocimetry (PIV) in an industrial environment, achieving an unprecedented level of flow-field resolution. A key contribution of this study is the identification of markedly different swirl distortion characteristics between separated intake flow conditions and those where only the ingested ground vortex is present. Local analysis at radially sensitive positions near the fan tip

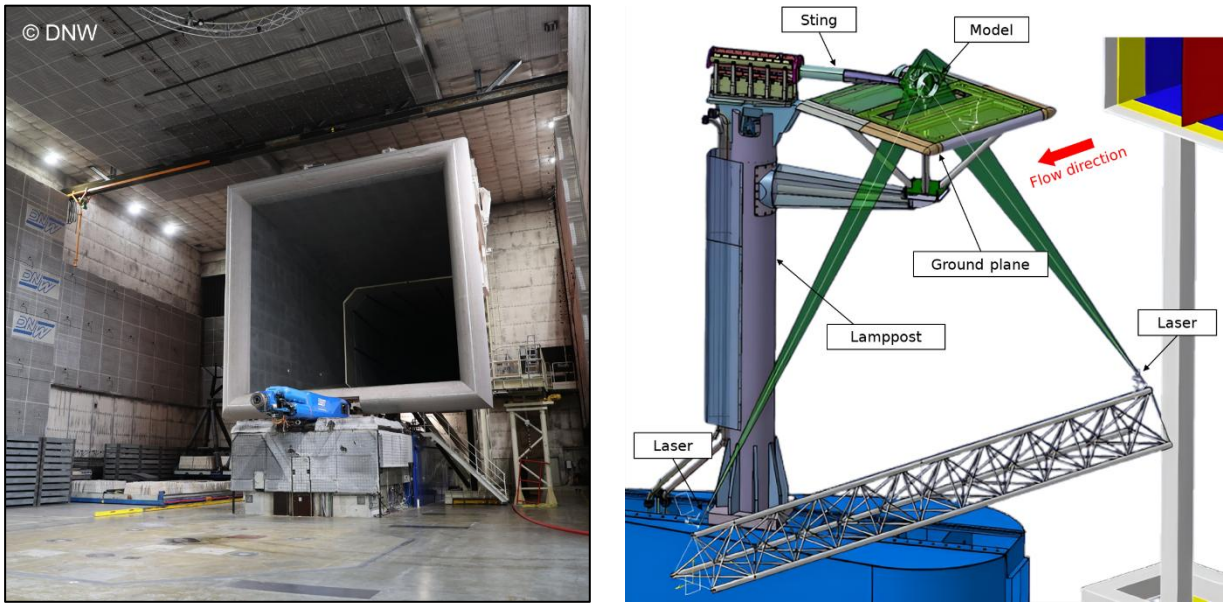
reveals that peak swirl distortion can differ substantially from global, area-averaged metrics. These high distortion levels indicate a potential reduction in rotor incidence angle and a corresponding decrease in fan performance, emphasizing the importance of considering both area-averaged and local swirl distortion values when evaluating intake-fan aerodynamic behavior. By employing PIV, fine spatial resolution across the plane can be obtained, in contrast to conventional rake-based techniques, thereby eliminating the need for intrusive probes and reducing experimental complexity.

The main impact of this work lies in its potential to redefine industry standards for intake-fan compatibility assessments. The proposed measurement and analysis framework enables resolution of flow features that were previously unmeasurable, representing a step-change in the ability to evaluate coupled intake-fan system performance. By moving beyond the limitations of intrusive distortion rakes, propulsion system designers can gain a more complete understanding of the full complexity of unsteady intake flows, enabling the development of more robust closely coupled fan-intake systems. Furthermore, the use of non-intrusive flow measurement techniques can enhance test productivity while providing improved prediction of extreme distortion levels.

III. Experimental Set-up and Methodology

A. Experimental Set-up and Operating Conditions

A concise summary of the experimental set-up is presented here for completeness; a full and detailed description is available in [39]. The experiments were conducted in the Large Low-speed Facility (LLF) of the German-Dutch Wind Tunnels (DNW). The facility operated with an open test section and a 6×6 m^2 contraction (Fig. 1a). A schematic overview of the experimental set-up is provided in Fig. 1b. The intake model was mounted along the wind-tunnel centerline using a sting connected to a lamppost type support structure. The lamppost was installed on a mobile, traversable turntable support system. This entire assembly, including the support system, lamppost, sting, model, and the ground plane used for crosswind tests, could be rotated as a single unit.



(a) (b)

Fig. 1 DNW-LLF experimental facility: (a) Photograph of the empty wind tunnel in open test-section configuration; (b) schematic of the test set-up.

The test article consisted of an intake representative of a generic high-bypass-ratio (HBPR) civil turbofan engine, integrated with a Turbine Powered Simulator (TPS) unit (Fig. 2). The intake geometry was developed using a cross-sectional profile of the NASA Common Research Model (CRM) nacelle [40]. The intake was designed to be axisymmetric, without droop or scarf, and was scaled to match the dimensions of the existing 10.2-inch (260 mm) diameter TPS fan rotor available at the DNW facility. The highlight diameter (D_{HL}) of the intake was 275 mm, and it

featured a length-to-inner-diameter ratio of L/D = 0.453. To ensure a fully turbulent boundary layer around the intake lip, boundary-layer trips were applied upstream of the highlight plane on the outer surface of the fan cowl.

The model was powered by a TPS unit comprising a single-stage fan with 19 rotor blades, 25 stator blades, and an elliptical spinner. The fan was driven by a turbine supplied with compressed air, which entered the system through a duct integrated into the support pylon (Fig. 2). The fan operating point during the experiment was monitored using rakes positioned in the bypass and core exhaust ducts. Several model components were coated in black paint to reduce light reflections during optical measurements, including all external nacelle surfaces, the intake lip, the TPS fan rotor and stator, the spinner, and the fan duct. For crosswind testing, the entire model assembly was rotated to 90° relative to the oncoming flow (Fig. 1b). In this configuration, the pylon and sting remained on the leeward side of the model to minimize interference with the flow approaching the intake.

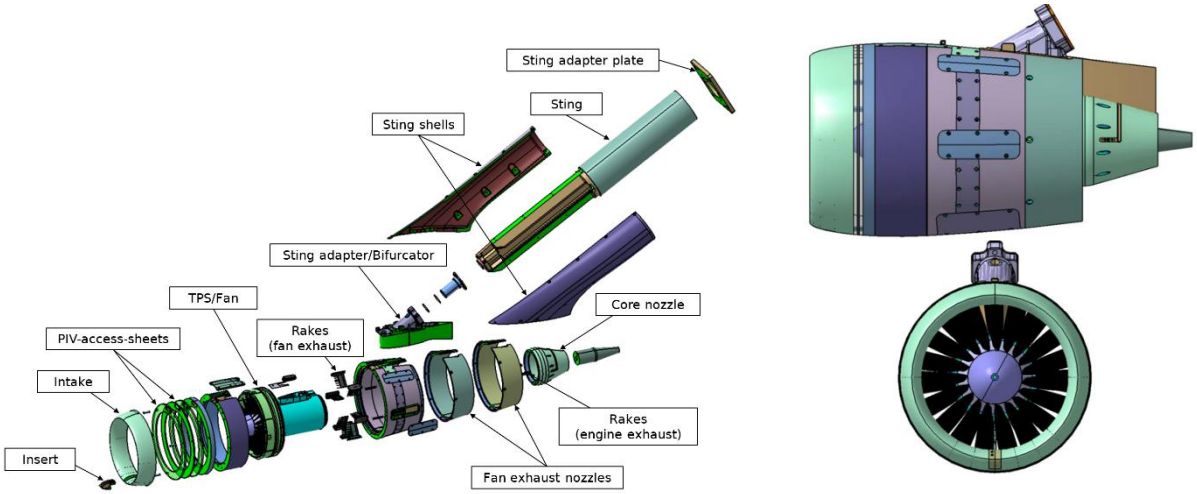
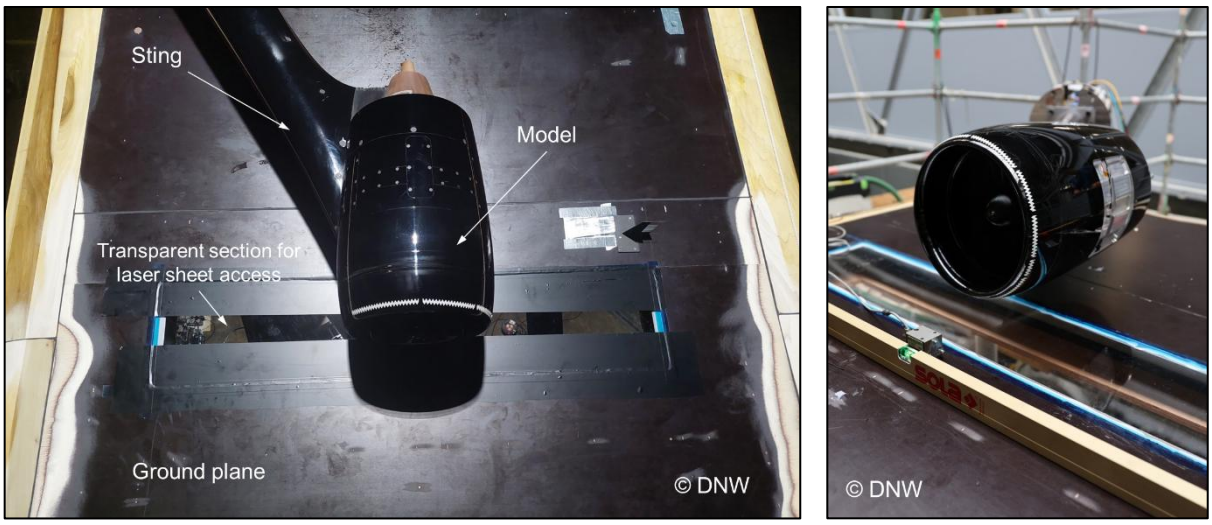


Fig. 2 Exploded and assembled views of the test article, illustrating the axisymmetric intake and the 10.2-inch TPS fan unit.

For simulating ground operations in crosswind conditions, a ground plane was attached to the lamppost extension via a pylon (Fig. 1b). The ground plane (Fig. 3a) had approximate dimensions of 2 m × 2 m, a thickness of 0.13 m, and a leading edge with a 2:1 elliptical profile. To promote boundary-layer transition on the upper surface, boundary-layer trips with a thickness of 0.79 mm and wedge angles of 60° were applied approximately 8 cm downstream of the leading edge. The ground plane was positioned at a fixed vertical distance h of 82.5 mm between its surface and the intake highlight bottom dead center (Fig. 3b). This corresponded to a fixed non-dimensional ground clearance of h/D_{HL} = 0.3.

The test conditions covered crosswind velocities ranging from 0 to 20 kts. The TPS operated at rotational speeds between 13,500 and 28,500 RPM, in increments of approximately 1,500 RPM. These conditions corresponded to ISA-normalized fan flow rates ranging from 4 to 8.3 kg/s, resulting in variations of the intake Mass Flow Capture Ratio ($MFCR = \dot{m}/\rho_\infty V_\infty A_{HL}$, [41]). The fan pressure ratio (FPR) ranged from 1.06 to 1.28. Two specific operating conditions are discussed in this paper; these are summarized in Table 1 and correspond to the cases also reported in [39].



(a) (b)

Fig. 3 Photographs of the model and ground plane: (a) Top view of the test article installed above the ground plane; (b) detail view showing the intake ground clearance.

Table 1 Operating conditions for the crosswind experiments with ground plane.

Case	V_∞ (kts)	RPM (kRPM)	$\dot{m}$ (kg/s)	FPR	$MFCR$
1	12.5	13.8	4.07	1.06	17.5
2	12.5	26.9	7.99	1.26	8.9

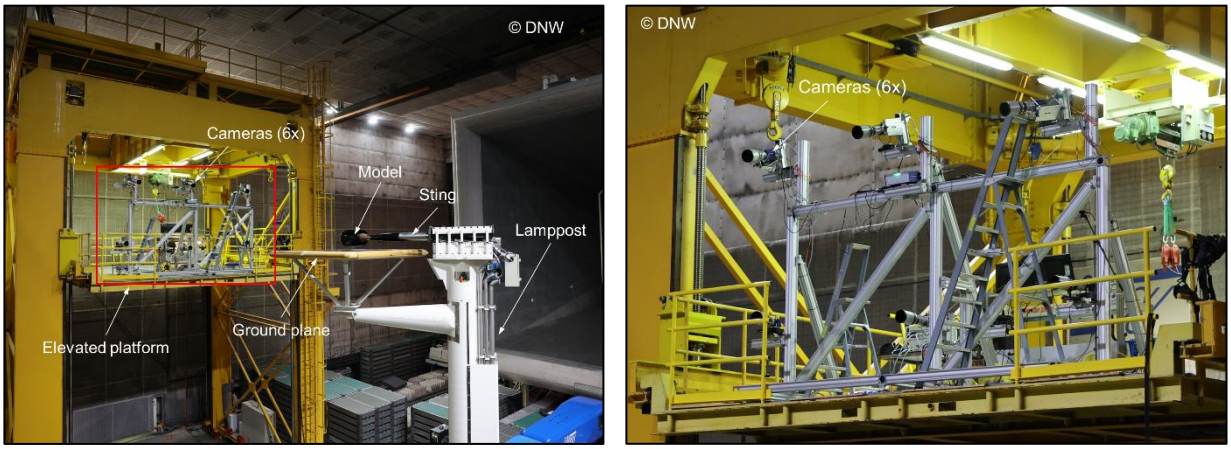
B. Stereoscopic PIV Set-up and Model Instrumentation

Stereoscopic Particle Image Velocimetry (S-PIV) measurements were acquired on a circular plane within the intake. This plane corresponded to a typical Aerodynamic Interface Plane (AIP) between the intake and the fan [42] and was positioned 30 mm upstream of the rotor entry section. The S-PIV set-up was similar to that described by Kempaiah et al. [37] and previously used for aspirated intake tests. Specifications of the PIV setup are provided in Table 2, with a brief description below.

The multi-camera system consisted of six LaVision Imager sCMOS cameras, each mounted on a motorized rotation unit enabling remote adjustment of focus and Scheimpflug angle. The cameras were arranged on a dedicated frame positioned on an elevated platform, aligned with the height of the model from the wind-tunnel floor (Fig. 4). Each camera was fitted with a 300 mm focal length lens, allowing imaging from a standoff distance of approximately 8.0 m from the measurement plane. The intake model featured a transparent ring to enable illumination of the measurement plane. Illumination was provided by two Quantel Evergreen dual-pulsed Nd:YAG lasers (532 nm, 2 × 200 mJ at 15 Hz), mounted beneath the ground plane on a linear traverse integrated into the support system (Fig. 1b). The laser beams were shaped into a light sheet using a set of lenses and mirrors and directed to the measurement plane through an acrylic window in the ground plane. The light sheets entered the intake from the lower left and lower right sides, minimizing shadowing caused by the fan spinner. This dual-laser configuration, also employed in the previous aspirated intake studies by Kempaiah et al. [37], was essential to achieve uniform illumination of the measurement plane. Flow seeding was performed using Di-Ethyl-Hexyl Sebacate (DEHS) particles, introduced into the main tunnel airflow via a seeding rake located in the tunnel's settling chamber.

Table 2 S-PIV technical specifications.

Function	Equipment	Specification
Imaging	Cameras	6 × LaVision Imager sCMOS
	Sensor resolution	2,560 × 2,160 px^2
	Recording method	Double frame/Single exposure
	Lens focal length	f = 300 mm
Illumination	Laser	2 × Quantel Evergreen Nd:YAG (532 nm, 2 × 200 mJ at 15 Hz)
Seeding	Tracer particles	Di-Ethyl-Hexyl Sebacate (DEHS)



(a) (b)

Fig. 4 (a) Photograph of the test set-up and elevated platform with the camera frame; (b) close-up view of the six PIV cameras mounted on the platform.

The double-frame/single-exposure PIV images were processed using LaVision's DaVis 11.0 software. All measurements were performed using a phase-locked set-up, synchronizing data acquisition with the fan's rotation to ensure that the blades consistently appeared at nearly the same azimuthal position throughout the dataset. The acquisition region measured 264 × 264 mm^2. Post-processing of the PIV images resulted in a final spatial resolution of approximately 2.5 mm^2 across the measurement plane for all test conditions. This resolution produced around 7,000 three-component velocity vectors within the region of interest, acquired at a temporal frequency of approximately 15 Hz. Each PIV dataset consisted of 1,000 snapshots. In the present analysis, only velocity data within the radial range $0.32R_{AIP} < r < 0.96R_{AIP}$ were considered to avoid possible spurious vectors near the intake and spinner surfaces. Velocity vectors were calculated using a cross-correlation technique with a multi-pass, window-refinement approach [43], employing a final interrogation window of 64 × 64 px^2 with 75% overlap (Table 3).

Table 3 S-PIV image processing parameters.

Parameter	
Correlation algorithm	Multi-pass dual-frame cross-correlation
Interrogation window	64 × 64 px^2
Overlap factor	75%

The intake model was also instrumented with a total of 234 steady pressure taps. These included 132 lip pressure taps distributed across nine circumferential locations at θ = 0°, 90°, 135°, 150°, 165°, 180°, 195°, 210°, and 270°, used for the calculation of the isentropic Mach number on the intake surface [45].

C. Assessment of Unsteady Swirl Distortion

Swirl distortion at the Aerodynamic Interface Plane (AIP) between the intake and the fan rotor was assessed by computing instantaneous swirl descriptors [44]. A similar approach was used in previous aspirated intake experiments [45]. For the calculation of the descriptors, the AIP was discretized into a polar grid consisting of 8 rakes equally distributed circumferentially and 5 concentric rings (Fig. 5).

The swirl angle was computed from the measured stereoscopic PIV velocity components as:

$$\alpha = tan^{-1}\left(\frac{v_\theta}{w}\right) \tag{1}$$

with v_θ circumferential velocity and w axial velocity components, respectively. Positive swirl angle was defined in the same direction as the fan rotor rotation (i.e., anticlockwise when viewed looking downstream). Two swirl descriptors were derived at each radial location i: the Swirl Intensity (SI, Eq. (2)), representing the magnitude of the swirl distortion based on the average absolute swirl angle across each ring, and the Swirl Directivity (SD, Eq. (3)), corresponding to the dominant rotational direction of the swirl distortion:

$$SI_i = \frac{SS_i^+\theta_i^+ + |SS_i^-|\theta_i^-}{360} \tag{2}$$

$$SD_i = \frac{SS_i^+\theta_i^+ + SS_i^-\theta_i^-}{SS_i^+\theta_i^+ + \left|SS_i^-\right|\theta_i^-} \tag{3}$$

with $SS_i^+$and SS_i^- positive and negative swirl angle sectors of extent θ_i^+ and θ_i^-, respectively. For each instantaneous snapshot, SI and SD values were calculated, and a spatial average across the five rings was used to obtain the overall swirl metrics at the AIP:

$$\overline{SI} = \frac{\sum_{i=1}^{5} SI_i A_i}{\sum_{i=1}^{5} A_i} \tag{4}$$

$$\overline{SD} = \frac{\sum_{i=1}^{5} SD_i A_i}{\sum_{i=1}^{5} A_i} \tag{5}$$

where A_i represents the area corresponding to each of the five rings.

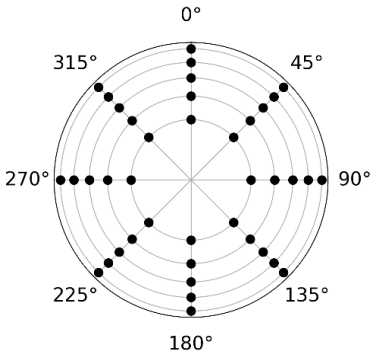


Fig. 5 8 × 5 rake used for the assessment of swirl distortion at the AIP, following SAE guidelines [44].

To better visualize the unsteady characteristics of the swirl distortion, joint probability density function (j-PDF) maps were generated. This visualization method, previously adopted by Gil Prieto et al. [46], illustrates how often specific combinations of swirl intensity and directivity occur, capturing unsteady or extreme distortion events that time-averaged metrics may overlook. The joint probability of observing specific swirl characteristics was computed as:

$$P[X_A \le X \le X_B, Y_A \le Y \le Y_B] = \int_{X_A}^{X_B}\int_{Y_A}^{Y_B} PDF\ dXdY \tag{6}$$

where X and Y represent the swirl descriptors (e.g., SI and SD), and A and B denote the minimum and maximum values of their range, respectively. The j-PDF was then normalized by the descriptors ranges.

D. Extreme Value Theory for Unsteady Flow Characterization

Unsteady swirl distortion at the Aerodynamic Interface Plane (AIP) can trigger rotating stall or engine surge, even when time-averaged distortion levels appear acceptable [47][48]. Industry practice often correlates stability margin penalties with the maximum expected distortion levels observed during testing [49]. Capturing representative peak values requires sufficiently long testing times, which may vary depending on the experimental set-up and scale of the test article. Testing durations are mostly determined based on prior experience and may fail to capture representative extreme distortion levels [50].

Extreme Value Theory (EVT) was introduced to estimate the maximum expected distortion levels, determine minimum test durations, and assess the associated uncertainties [51]. In this study, EVT was applied to predict the peak swirl distortion at the AIP beyond the testing window for the two operating conditions considered. Originally formulated by Jacocks [52] and first applied to inlet distortion by Jacocks and Kneile [50], EVT has primarily been used in intake distortion studies to assess peak swirl intensity in S-ducts [53][54]. In this work, EVT was implemented using the Peak-Over-Threshold (POT) approach (Fig. 6), following the methodology described by Coles [55]. In this method, values X_i of a generic distortion parameter X that exceed a selected threshold U_t are considered as exceedances:

$$Y_i = (X_i - U_t)|_{X_i > U_t} \tag{7}$$

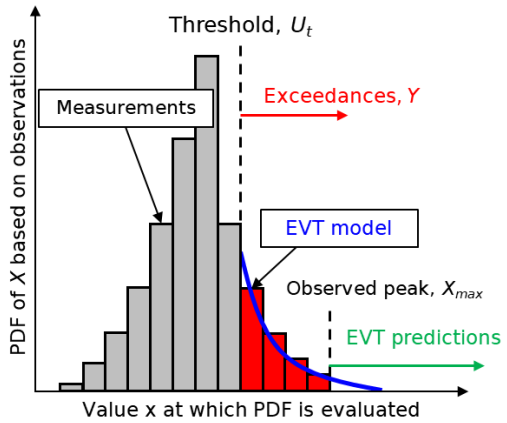


Fig. 6 Extreme Value Theory (EVT) framework showing the Peak-Over-Threshold (POT) approach.

For a sufficiently high threshold and large sample size, the distribution of exceedances can be modelled using a Generalized Pareto Distribution (GPD). The shape (ξ) and scale (χ) parameters of the GPD can be estimated via the Maximum Likelihood Method (MLM) [56], by maximizing the log-likelihood function:

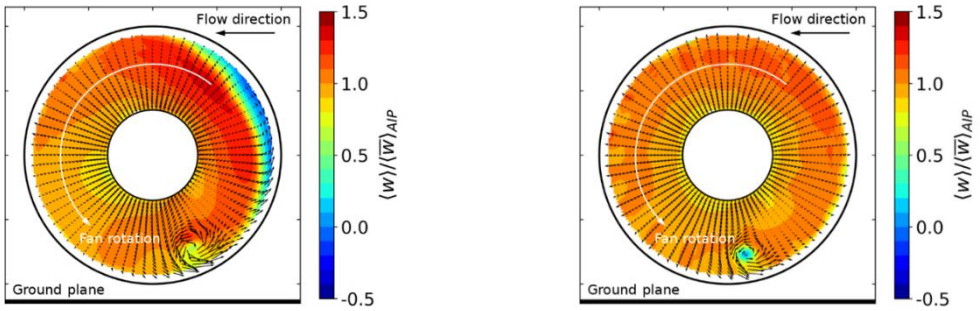
$$logL(\xi, \chi) = -klog(\chi) - (1 + 1/\xi) \sum_{i=1}^{k} \log\left(1 + \frac{\xi Y_i}{\chi}\right) \tag{8}$$

where k is the number of exceedances. For $\xi < 0$, the distribution of the exceedances is asymptotic and bounded by the value $U_b = U_t - \chi/\xi$, known as upper bound. Once the model parameters ξ and χ are determined, the peak value x_m (known as the m-observation return level) can be estimated. The threshold U_t was determined using the Shape-Estimates-Over-A-Range-Of-Thresholds method, which minimizes the root-mean-square error between measured and predicted quantiles, as recommended by Coles [55]. The results of the EVT prediction are presented using return level plots, including the associated uncertainty intervals. Model accuracy was assessed using probability–probability (P-P) and quantile-quantile (Q-Q) plots.

IV. Results and Discussion

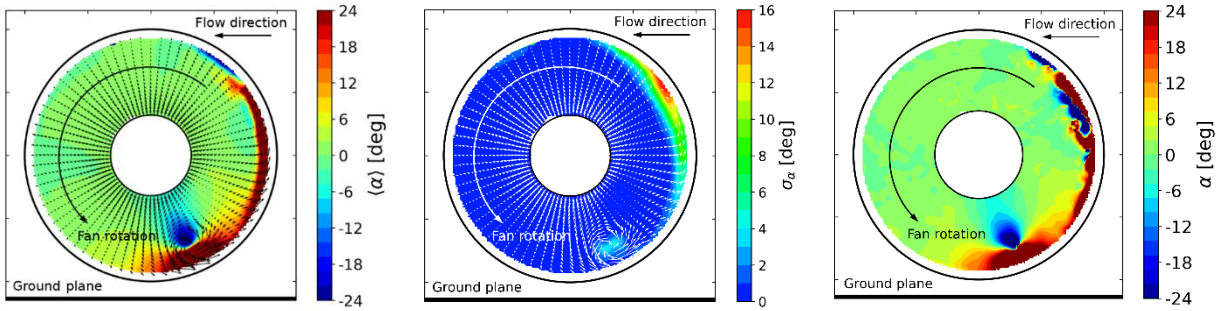
A. Axial Velocity and Swirl Angle Distributions at the Aerodynamic Interface Plane

The analysis presented in this section builds upon the measured data previously reported in [39][57]. The time-averaged, normalized axial velocity distributions for the two operating conditions considered, both at a crosswind velocity of 12.5 kts but at different fan speeds and intake $MFCR$, are shown in Fig. 7a (Case 1 in Table 1) and Fig. 7b (Case 2 in Table 1). Corresponding swirl angle distributions, including time-averaged values, standard deviation, and representative instantaneous snapshots, are presented in Fig. 8 and Fig. 9. The instantaneous velocity fields from the S-PIV measurements were used to compute the time-averaged distributions. In-plane velocity vectors are superimposed on the axial velocity and swirl angle distributions.



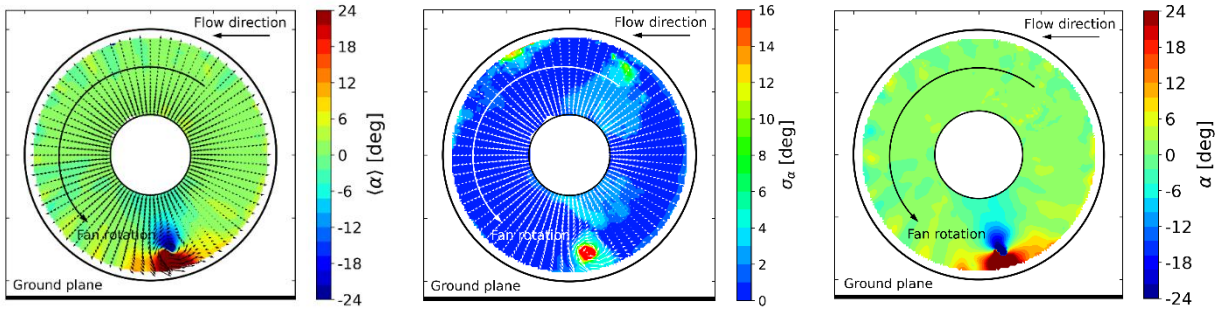
(a) (b)

Fig. 7 Time-averaged, normalized out-of-plane velocity distributions at the Aerodynamic Interface Plane (AIP) for Case 1 (a) and Case 2 (b).



(a) (b) (c)

Fig. 8 Time-averaged (a), standard deviation (b), and instantaneous (c) swirl angle distributions at the Aerodynamic Interface Plane (AIP) for Case 1 (V∞=12.5 kts | 13.5 kRPM | MFCR=8.9).



(a) (b) (c)

Fig. 9 Time-averaged (a), standard deviation (b), and instantaneous (c) swirl angle distributions at the Aerodynamic Interface Plane (AIP) for Case 2 (V∞=12.5 kts | 26.5 kRPM | MFCR=17.5).

At a fan speed of 13.5 kRPM, the intake operates at a low $MFCR$. In this case, diffusion-induced flow separation develops along the windward inner surface of the intake, evidenced by a localized region of negative axial velocity (Fig. 7a). A co-rotating ground vortex is visible in both the axial velocity (Fig. 7a) and swirl angle (Fig. 8) distributions. The nature of the flow separation in this case was confirmed by examining the isentropic Mach number distributions on the inner surface of the intake [57], which are not reported here for brevity. Values below unity were observed at this operating condition, confirming the low-speed nature of the separation.

At higher $MFCR$, corresponding to a fan speed of 26.5 kRPM, the intake flow remains attached on the windward inner lip (Fig. 7b). The co-rotating ground vortex, induced by the crosswind and the proximity of the ground plane, is also present under this operating condition (Fig. 9). The observed flow topologies are consistent with previous experiments conducted at similar operating conditions for an aspirated intake configuration [45], where the intake transitioned between diffusion-driven separation at low $MFCR$ and attached flow at higher $MFCR$.

The time-averaged and instantaneous swirl angle distributions for the two operating conditions show absolute swirl angles exceeding 30° in regions influenced by the ground vortex and/or reversed flow (Fig. 8 and Fig. 9). In the tip region, both the ground vortex and the separated flow contribute to anticlockwise (co-rotating) swirl, which tends to decrease the rotor blade incidence. Closer to the hub, the dominant contribution arises from the counter-rotating portion of the ground vortex. In this region, large negative swirl angles indicate strong clockwise rotation, leading to a local increase in incidence at the rotor leading edge. This is observed for both operating points, regardless of whether the flow is separated at low $MFCR$ (13.5 kRPM, $MFCR$ = 8.9) or attached at higher $MFCR$ (26.5 kRPM, $MFCR$ = 17.5).

B. Swirl Distortion Assessment Using Stereoscopic PIV Data

A statistical assessment of the area-averaged absolute swirl angle at the Aerodynamic Interface Plane (AIP) for the two test cases at 12.5 kts provides a quantitative measure of both the time-averaged and unsteady swirl distortion levels at these operating points (Table 4).

Table 4 Statistics of the area-averaged absolute swirl angle at the AIP.

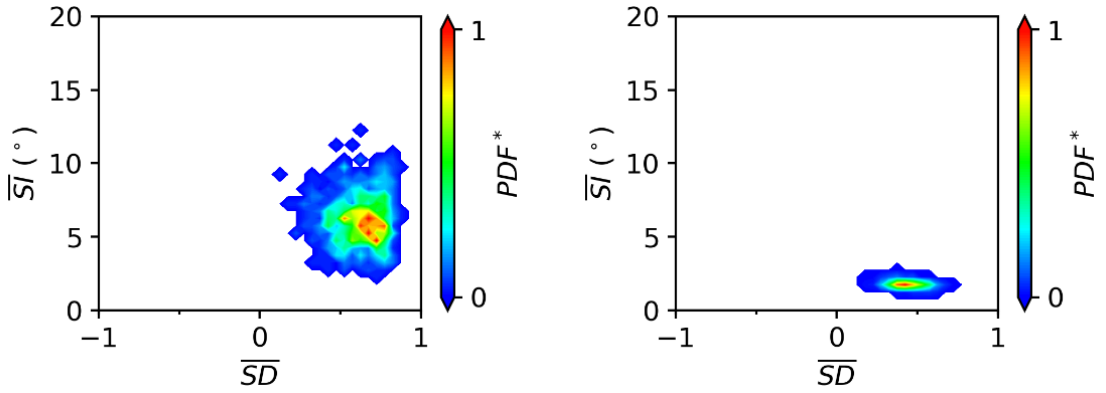
	$\overline{\lvert\alpha\rvert}_{avg}$ (°)	$\overline{\lvert\alpha\rvert}_{std}$ (°)	$\overline{\lvert\alpha\rvert}_{min}$ (°)	$\overline{\lvert\alpha\rvert}_{max}$ (°)
Case 1	7.3	1.7	2.7	12.5
Case 2	1.9	0.2	1.5	2.9

The comparison between the two conditions, with attached (26.5 kRPM, $MFCR$ = 17.5) and separated flow (13.5 kRPM, $MFCR$ = 8.9), highlights significant differences in the magnitude of the absolute swirl angle and the potential impact on fan rotor performance. In the attached-flow case, the time-averaged, minimum, and maximum values of the area-averaged absolute swirl angle are all substantially lower than in the separated-flow case. This observation is consistent with the time-averaged and fluctuating swirl angle distributions shown in Fig. 8a and Fig. 8c. Even with the presence of the ground vortex, which locally produces swirl angle peaks 6-8 times larger than those in the remainder of the AIP, the area-averaged and maximum absolute swirl angles remain below the 10° threshold referenced in the literature [44][58], although this limit is known to be design-dependent. This indicates that, for the attached-flow condition, the overall flow entering the fan remains relatively uniform despite the localized non-uniformity associated with the ingested ground vortex.

In contrast, for the separated-flow case characterized by diffusion-driven separation (13.5 kRPM, $MFCR$ = 8.9), the area-averaged absolute swirl angle increases significantly. The time-averaged and maximum values reach 7.3° and 12.5°, respectively. These elevated distortion levels indicate that separated flow leads to a more adverse aerodynamic conditions at the AIP. As noted in previous studies involving an aspirated intake [45], operating points dominated by diffusion-driven separation tend to generate high area-averaged swirl distortion, a behavior that is also observed here despite the presence of the fan.

A more comprehensive assessment of the swirl distortion at the AIP is achieved by evaluating both the overall magnitude and the predominant direction of the swirling flow, as proposed in [44]. This approach makes it possible to relate the strength of the swirl distortion to its directional characteristics. These are directly linked to the incidence angle at the rotor blade leading edge which determines whether the blade loading increases or decreases depending on whether the flow is co-rotating or counter-rotating with respect to the rotor motion [59]. To quantify this, the area-averaged swirl intensity $\overline{SI}$ and the area-averaged swirl directivity $\overline{SD}$ were calculated. While the statistical properties of these parameters, such as the time-average and standard deviation, summarized in Table 5 for both operating conditions provide a quantitative description of the average swirl distortion, it is equally important to assess its

variability and the occurrence of peak distortion events. To this end, the joint Probability Density Function (j-PDF) maps of $\overline{SI}$ and $\overline{SD}$ were generated (Fig. 10). The range of the descriptors was discretized into 40 equally spaced bins, resulting in a resolution of 0.5° for $\overline{SI}$ and 0.05 for $\overline{SD}$.



(a) (b)

Fig. 10 Area-averaged SD-SI j-PDF maps for (a) Case 1 (V∞=12.5 kts | 13.5 kRPM | MFCR=8.9) and (b) Case 2 (V∞=12.5 kts | 26.5 kRPM | MFCR=17.5).

Table 5 Area-averaged swirl intensity statistical properties.

	$\overline{SI}_{avg}$ (°)	$\overline{SI}_{std}$ (°)	$\overline{SI}_{min}$ (°)	$\overline{SI}_{max}$ (°)
Case 1	6.1	1.6	2.4	11.4
Case 2	1.8	0.2	1.3	2.5

At 13.5 kRPM and $MFCR$ = 8.9, the swirl intensity ($\overline{SI}$) shows significant spatial and temporal variability (Fig. 10a), with a time-averaged value $\overline{SI}_{avg}$ of 6.1° and a maximum value $\overline{SI}_{max}$ of 11.4°, approximately twice the average (Table 5). These results are consistent with the area-averaged absolute swirl angle statistics discussed earlier (Table 4). The swirl direction in this case is predominantly co-rotating with the fan, as evident from the time-averaged and instantaneous swirl angle distributions (Fig. 8). This is associated with the high positive swirl angles in the regions affected by the ground vortex and the separated flow. The resulting swirl directivity ($\overline{SD}$) indicates a possible net reduction in incidence at the rotor blade leading edge, which may significantly decrease the fan mass flow rate and pressure ratio, as shown in earlier studies [44].

At higher fan speed and $MFCR$, the swirl intensity is notably lower, with $\overline{SI}_{avg}$ = 1.8° and $\overline{SI}_{max}$ = 2.5° (Table 5). This case exhibits a more uniform flow field and reduced unsteadiness compared to the separated-flow condition, as reflected in the lower standard deviation ($\overline{SI}_{std}$) and the tighter clustering of values in the $\overline{SD}$-$\overline{SI}$ map (Fig. 10b). The lower swirl distortion and unsteadiness result from the absence of reversed flow and the stabilizing influence of the fan, which helps redistribute the flow and suppress separation at relatively high $MFCR$, even though the flow is still affected by the presence of the ground vortex (Fig. 9).

A similar analysis was carried out at a specific radial position across the Aerodynamic Interface Plane (AIP). This evaluation is particularly useful for identifying the magnitude and direction of swirl distortion in regions that are especially critical for the fan rotor, such as the blade tip. Extreme distortion events in this area are known to potentially trigger blade stall, which can severely compromise aero-engine stability and operability [59]. Therefore, as previously done on an area-averaged basis, it is important not only to quantify the magnitude of the local swirl intensity (SI) at this radial location but also to assess the directionality of the distortion in terms of swirl directivity (SD). In the present coupled fan/intake configuration, regions of high swirl angle were observed near the intake surface close to the fan tip, where the ingested ground vortex and local flow separation occur (Fig. 8 and Fig. 9). Although the fan blade tip region is only assumed to be the most sensitive to instability onset, the analysis was nonetheless performed at a radial position close to the blade tips.

The j-PDF maps of SD and SI for the two operating conditions at 12.5 kts, evaluated at a normalized radial position of r/R_{AIP} = 0.956 (outermost ring in Fig. 5), are shown in Fig. 11a and Fig. 11b, respectively. A summary of the SI

statistics for both cases is provided in Table 6. The joint Probability Density Function (j-PDF) maps were computed by discretizing the range of each descriptor into 40 equally spaced bins, providing a resolution of 1° for SI and 0.05 for SD.

For the operating condition characterized by diffusion-driven separation at $MFCR$ = 8.9 and a fan speed of 13.5 kRPM (Fig. 11a), the SD–SI j-PDF map exhibits a distribution spanning $-1 < SD < 1$, covering both the counter-rotating ($-1 < SD < 0$) and co-rotating ($0 < SD < 1$) regions of the plot. Swirl intensity values reach up to 40°, indicating high levels of localized distortion. This quasi-symmetric distribution reflects the swirl angle pattern observed in the reversed-flow region (Fig. 8). However, the co-rotating swirl associated with the ground vortex and the separated flow tends to dominate, with the highest SI values clustered in the $0 < SD < 1$ region.

In contrast, at higher $MFCR$ and fan speed (Fig. 11b), the SD–SI distribution becomes significantly more clustered within the co-rotating the region, with SI values remaining below 10°. This indicates a substantial reduction in both local swirl distortion intensity and unsteadiness at this radial location, despite the presence of the co-rotating ground vortex.

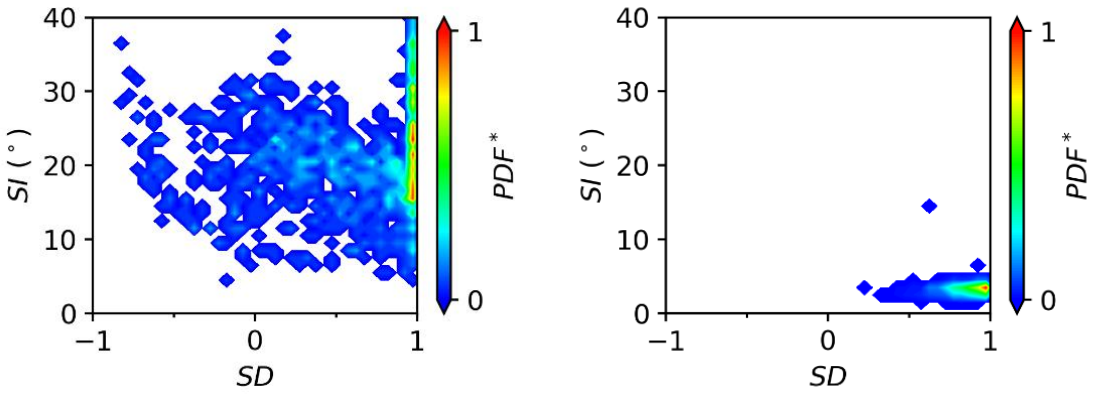


Fig. 11 SD-SI j-PDF maps for (a) Case 1 (V∞=12.5 kts | 13.5 kRPM | MFCR=8.9) and (b) Case 2 (V∞=12.5 kts | 26.5 kRPM | MFCR=17.5) evaluated at r/R$_{AIP}$ = 0.956.

Table 6 Statistical properties of the local swirl intensity evaluated at r/R$_{AIP}$ = 0.956.

	SI_{avg} (°)	SI_{std} (°)	SI_{min} (°)	SI_{max} (°)
Case 1	20.8	7.1	4.3	46.8
Case 2	3.3	0.6	1.7	14.7

The analysis of the joint probability density function (j-PDF) maps for area-averaged descriptors, compared to those for local descriptors, shows that the variability at specific r/R_{AIP} locations differs substantially from the variability and unsteadiness observed when quantities are averaged over the entire AIP. This highlights the importance of considering both area-averaged and local swirl distortion metrics in the assessment of the aerodynamic performance of an intake or fan. The area-averaged values are related to the overall fan performance parameters such as mass flow, pressure ratio, and isentropic efficiency [58], whereas the local values are linked to the actual flow incidence at the rotor blade leading edge and are therefore directly associated with the onset of blade stall. Consequently, measurement techniques capable of providing high spatial resolution across the AIP, such as PIV, are essential.

C. Prediction of Peak Swirl Distortion Values

Current industry practice most often relies on time-averaged evaluations of AIP flow distortions. However, as demonstrated previously, unsteady flow conditions, particularly under separated intake flow regimes, can exhibit instantaneous swirl intensity values that far exceed time-averaged values. Such extreme values of flow distortion may trigger aerodynamic instabilities even when the mean distortion level remains below the fan rotor distortion-tolerance threshold [34][47]. Previous studies have also noted that these peak distortion events may go undetected during experiments due to the random nature of unsteady flow distortion [50]. Consequently, the likelihood of capturing peak events during an engine compatibility test increases with the duration of data acquisition. In large-scale industrial wind

tunnels, however, long acquisition times are often impractical due to time and cost constraints. As a result, a significant residual risk may remain because the propulsion system may not be exposed to representative extreme distortion events. To address this challenge, statistical approaches such as Extreme Value Theory (EVT) are increasingly being used to predict peak distortion levels using experimental datasets of limited duration.

In this study, EVT was applied to swirl distortion data obtained from Stereoscopic Particle Image Velocimetry (S-PIV) measurements at the AIP of a coupled fan/intake system operating under crosswind conditions. To the best of the authors' knowledge, this represents the first application of EVT to such a configuration in the open literature. The EVT model was used to estimate both the peak area-averaged swirl intensity ($\overline{SI}_{peak}$) and the local swirl intensity (SI_{peak}), thereby providing insight into the maximum distortion levels that a fan rotor may encounter at the AIP under the tested conditions. For the present analysis, the peaks of the area-averaged and local swirl intensity were computed using the 1,000 PIV snapshots ($m = 10^3$) acquired at each of the two operating conditions: one characterized by separated flow, and the other by attached flow in which the ingested ground vortex was the dominant source of distortion. Each dataset corresponds to approximately one minute of acquisition time. To assess the potential variability in expected peak values associated with flow separation and ground vortex effects, the EVT model was extrapolated to a dataset of two orders of magnitude larger ($m = 10^5$), equivalent to roughly two hours of continuous acquisition. In addition to peak predictions, EVT was also used to estimate the upper bound (i.e., the asymptotic limit, U_b) and the associated 95% confidence interval, following the methodology previously described by Gil-Prieto et al. [53] and Migliorini et al. [54].

The EVT was first applied to the area-averaged $\overline{SI}$ datasets. A summary of the EVT model parameters used for peak prediction under the two operating conditions considered is provided in Table 7. The return level plots of the area-averaged swirl intensity $\overline{SI}$ or the two cases at 12.5 kts (Fig. 12a and Fig. 13a) illustrate the relationship between the experimental peak value $\overline{SI}_{peak,exp}$ and the predicted peak value for a dataset of $m = 10^5$ observations ($\overline{SI}_{m=10^5}$). Each figure also includes the 95% confidence intervals and the empirical data. The diagnostic plots used to assess the accuracy of the EVT fitting are presented in Fig. 12b and Fig. 13b, respectively, and indicate that the method has fully converged with respect to the evaluated properties. The results are summarized in Table 8, which reports the experimental peak values observed from datasets of 1,000 snapshots, the EVT-predicted peak values with associated 95% confidence intervals, and the estimated upper bounds of the $\overline{SI}$ distribution.

Table 7 Parameters of the EVT model used for estimating the peak values of area-averaged swirl intensity. The parameters include the shape parameter (ξ), scale parameter (χ), number of exceedances (k), mean of the distribution (μ), and the threshold (U_t).

	ξ	χ	k	μ (°)	U_t (°)
Case 1	-0.1997	0.975	77	6.1	8.6
Case 2	-0.0642	0.0955	72	1.8	2.0

At the lower fan speed and $MFCR$ condition, characterized by diffusion-driven separation (Case 1 in Table 1), the EVT model was fitted to the distribution of experimental peak $\overline{SI}$ values (Fig. 12), with the upper bound lying within the predicted confidence intervals. At this operating point, the fan/intake system experiences a spatially extensive flow separation, as discussed previously. The experimental peak wirl intensity $\overline{SI}_{peak,exp}$ is 11.4°, while the predicted value $\overline{SI}_{m=10^5}$ is 12.7° ± 1.6°. This indicates that under such flow conditions, the peak $\overline{SI}$ could be up to 11% higher than the experimentally observed maximum. The estimated upper bound (U_b = 13.5°) is approximately 18% higher than $\overline{SI}_{peak,exp}$.

For the higher $MFCR$ condition (Case 2 in Table 1), the difference between $\overline{SI}_{peak,exp}$ and $\overline{SI}_{m=10^5}$ reduces to approximately 8% (Table 8), confirming a more stable flow. $\overline{SI}_{peak,exp}$ decreases to 2.5°, with an EVT-predicted value of 2.7° ± 0.4° and an upper bound of 3.5°. Although the upper bound falls outside the confidence interval (Fig. 13), suggesting slightly reduced model accuracy, the relatively small difference between experimental and predicted peak values implies that extending the dataset beyond 1,000 snapshots would offer only marginal improvements. Given that the flow is predominantly attached, longer data acquisition would require more resources without significantly enhancing accuracy, especially since noise and small-scale disturbances under attached flow conditions may influence the EVT prediction.

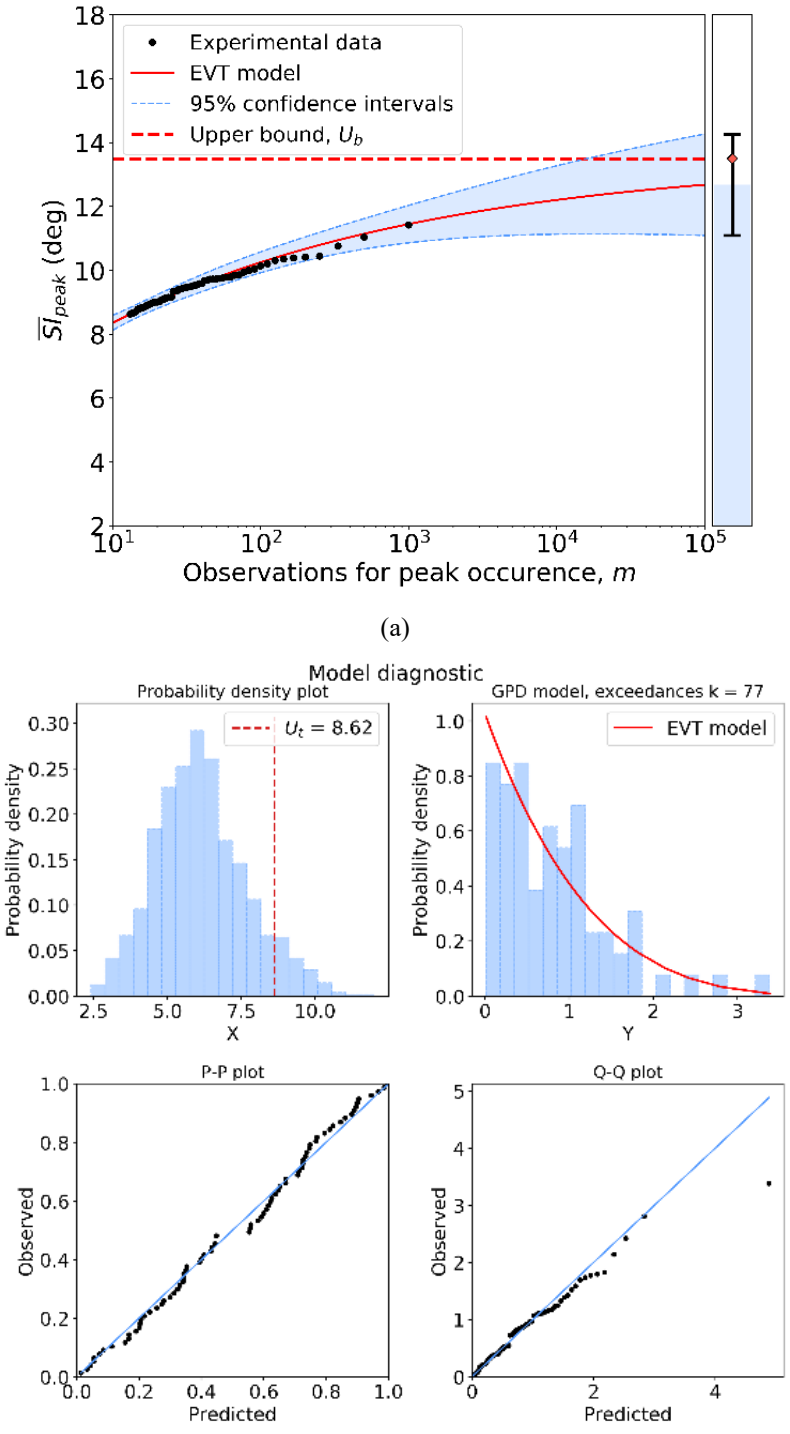
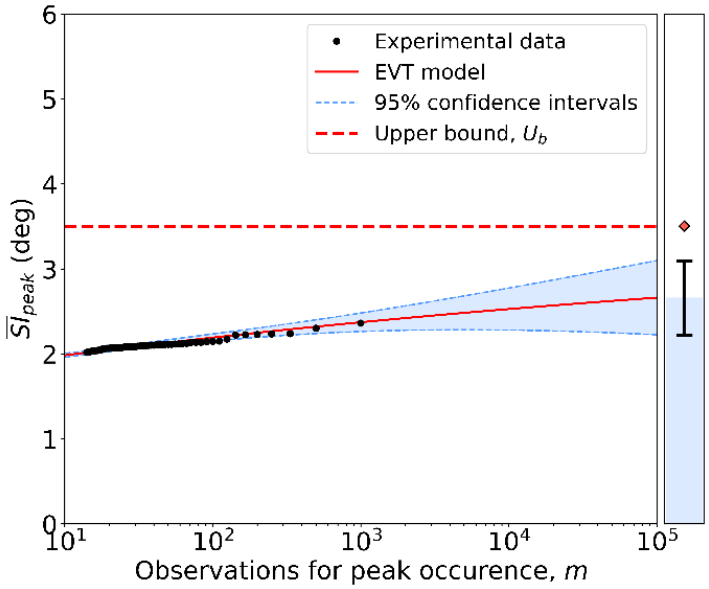
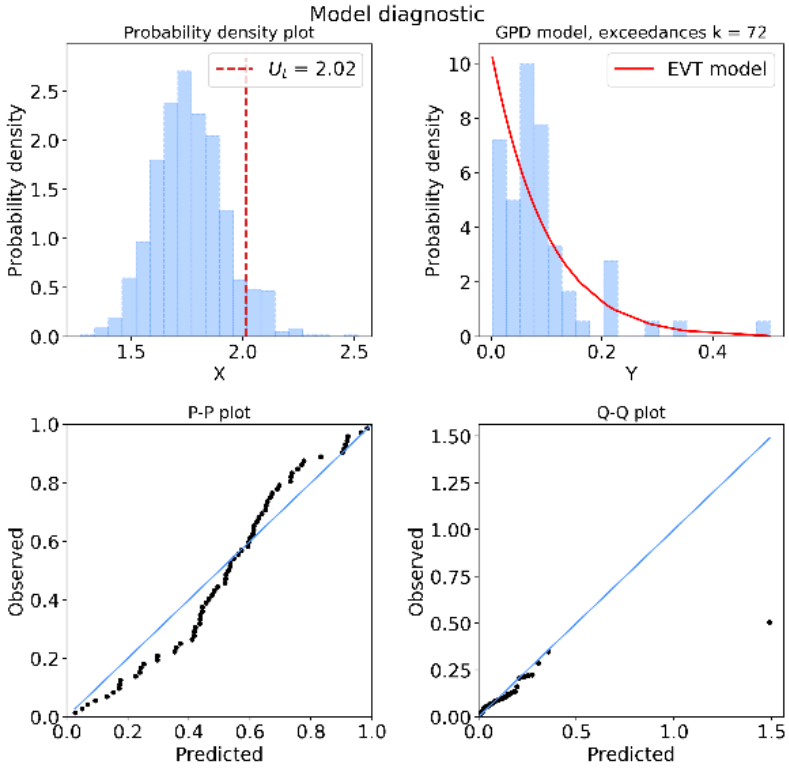


Fig. 12 (a) EVT return level plot of the peak area-averaged swirl intensity for Case 1 (V∞=12.5 kts | 13.5 kRPM | MFCR=8.9). (b) Diagnostic plots for the EVT model.



(a)



(b)

Fig. 13 (a) EVT return level plot of the peak area-averaged swirl intensity for Case 2 (V∞=12.5 kts | 26.5 kRPM | MFCR=17.5). (b) Diagnostic plots for the EVT model.

Table 8 Experimental and EVT-predicted values of the peak area-averaged swirl intensity.

	$\overline{SI}_{peak,exp}$ (°)	$\overline{SI}_{m=10^5}$ (°)	U_b (°)
Case 1	11.4	12.7 ± 1.6	13.5
Case 2	2.5	2.7 ± 0.4	3.5

Overall, the experimental peak values obtained from 1,000 snapshots provided a reasonably accurate estimate of the peak swirl distortion levels at both operating conditions. However, longer testing would be required in separated flow cases to reduce the confidence intervals of the EVT predictions and obtain a more precise estimate of the expected maximum distortion levels. In contrast, for attached flow conditions, where the ingested ground vortex is the primary source of distortion, the EVT offers little additional benefits beyond the already measured peak values. These findings suggest that testing efforts should focus primarily on separated flow scenarios characterized by diffusion-driven separation in order to capture the full range of peak distortion levels and achieve a more comprehensive characterization of swirl distortion.

As shown, although the peak values of the area-averaged swirl intensity provide a useful measure of the overall magnitude of swirl distortion across the AIP, spatial averaging across the plane can obscure the localized distortion peaks. These local peaks may have a significant impact on aero-engine operability and performance, as they directly influence the incidence angle at the rotor blade leading edge, either increasing or decreasing it depending on the swirl direction. Therefore, it is essential to evaluate the expected maximum swirl distortion at radial locations where local effects are most critical, particularly in regions influenced by the ingested ground vortex and flow separation, i.e. near the intake inner surface close to the fan blade tip. To this end, EVT was applied to predict the peak swirl intensity at a radial position of r/R_{AIP} = 0.956 (Fig. 14 and Table 9), representative of the blade tip region where instabilities are more likely to occur and may potentially trigger stall.

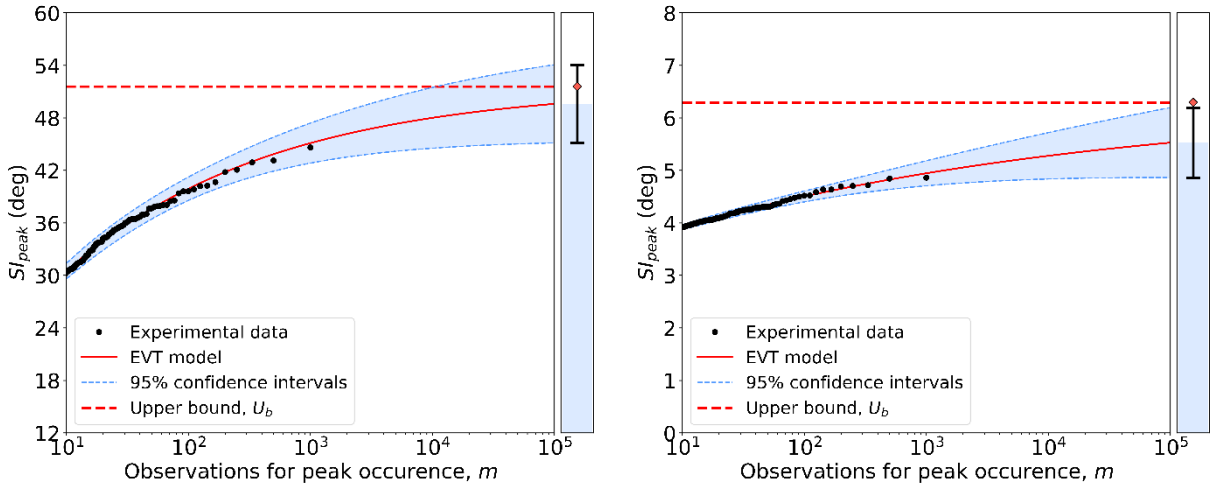


Fig. 14 EVT return level plots of the peak swirl intensity evaluated at r/R_{AIP} = 0.956. for (a) Case 1 (V∞=12.5 kts | 13.5 kRPM | MFCR=8.9) and (b) Case 2 (V∞=12.5 kts | 26.5 kRPM | MFCR=17.5).

Table 9 Experimental and EVT-predicted values of the peak swirl intensity evaluated at r/R_{AIP} = 0.956.

	$SI_{peak,exp}$ (°)	$SI_{m=10^5}$ (°)	U_b (°)
Case 1	44.6	49.6 ± 4.5	51.6
Case 2	4.9	5.5 ± 0.7	6.3

The EVT model demonstrated good agreement with the distribution of measured exceedances and converged successfully, allowing the estimation of local maximum swirl distortion levels under both separated and attached flow conditions. In the separated-flow case at 13.5 kRPM and $MFCR$ = 8.9 (Fig. 14a), the experimental peak swirl intensity was 44.6°, while EVT predicted a maximum of 49.6° ± 4.5°, with an upper bound of 51.6° (Table 9**)**. This indicates that local swirl distortion at this operating point may exceed measured values and reach levels that are potentially more critical for the fan rotor. In contrast, under the attached-flow condition at 26.5 kRPM and $MFCR$ = 17.5 (Fig. 14b), the experimental peak swirl intensity was significantly lower, consistent with earlier observations. The EVT model predicted a maximum value of 5.5° ± 0.7°, with an upper bound of 6.3° (Table 9), likely remaining below the levels critical for fan rotor stability, although a detailed performance analysis would be required to confirm this. Overall, applying EVT to local swirl descriptors demonstrates its value in estimating peak swirl distortion from relatively limited datasets (here, 1,000 S-PIV snapshots). The results highlight that relying solely on time-averaged or conventional statistical metrics can substantially underestimate the severity of local flow distortions at the AIP of a coupled intake/fan system operating in crosswind conditions.

As observed from the j-PDF maps and the measured descriptors, the EVT return plots indicate that predicted peak distortion at specific local r/R_{AIP} positions can differ substantially from predictions based on area-averaged descriptors. This underscores the importance of considering both area-averaged and local swirl distortion metrics when evaluating the performance of coupled fan–intake systems, as local positions along the blade span may experience markedly higher distortion levels. Such localized peaks have the potential to induce blade stall but are obscured when only area-averaged descriptors are considered. Therefore, measurement techniques with high spatial resolution across the plane, such as Particle Image Velocimetry (PIV), are essential for a comprehensive assessment of swirl distortion and for enabling detailed local flow analysis.

V. Conclusions

This study analyzed Stereoscopic Particle Image Velocimetry (S-PIV) data acquired across a cross-flow plane within an aero-engine intake operating in crosswind, featuring a ground plane and a co-rotating ground vortex upstream of a rotating fan. Two operating conditions were examined: one with diffusion-driven separation at low fan speed and Mass Flow Capture Ratio ($MFCR$), and another with attached flow at higher fan speed and $MFCR$. Swirl distortion at the Aerodynamic Interface Plane (AIP) was significantly higher in the separated-flow case, with time-averaged and peak values up to three and four times greater, respectively, than in the attached-flow case, where only the ingested ground vortex was present. These high distortion levels, particularly near the fan tip, indicate potential reductions in rotor incidence angle and fan performance. Maximum instantaneous swirl reached approximately twice the time-averaged level, highlighting the limitations of relying solely on time-averaged or area-averaged descriptors. For the first time, Extreme Value Theory (EVT) was applied to swirl descriptors for such a configuration, predicting peak values 10-20% above the experimental maxima.

This work demonstrates a fully non-intrusive, high-resolution methodology capable of characterizing swirl distortion within a representative intake-fan system, enabling more complete evaluations of intake-engine performance. The novelty of this approach lies in combining detailed swirl distortion descriptors from PIV with EVT-based predictions of extreme peak values, allowing estimation of rare distortion events. A key contribution is the demonstration that local distortion analysis at radially sensitive positions near the fan tip provides deeper insight into peak swirl distortion than metrics averaged across the entire fan face. Unlike conventional rake-based techniques, this methodology reduces the need for intrusive measurements in engine compatibility assessments. The impact of this approach lies in its potential to reshape industry practices by enabling detailed, non-intrusive evaluation of unsteady flow distortion, optimizing testing durations, and improving the prediction of extreme distortion levels.

Acknowledgments

The work presented herein was conducted under the NIFTI project which received funding from the Clean Sky 2 Joint Undertaking (JU) under Grant Agreement No 864911. The authors would like to thank German-Dutch Wind Tunnels (DNW) and LaVision GmbH for generating and providing the velocity data used in this study as part of the NIFTI project.

References

[1] Birch, N. T., "2020 Vision: The Prospects for Large Civil Aircraft Propulsion," *The Aeronautical Journal*, Vol. 104, No. 1038, 2000, pp. 347–352. doi: 10.1017/S0001924000063971

[2] Owens, R., Hasel, K., and Mapes, D., "Ultra High Bypass Turbofan Technologies for the Twenty-First Century," AIAA Paper 1990-2397, 1990.
doi: 10.2514/6.1990-2397

[3] Hughes, C., Van Zante, D., and Heidmann, J., "Aircraft Engine Technology for Green Aviation to Reduce Fuel Burn," AIAA Paper 2011-3531, 2011.
doi: 10.2514/6.2011-3531

[4] Daggett, D., Brown, S., and Kawai, R., "Ultra-Efficient Engine Diameter Study," NASA CR, 2003.

[5] Peters, A., Spakovszky, Z. S., Lord, W. K., and Rose, B., "Ultrashort Nacelles for Low Fan Pressure Ratio Propulsors," *Journal of Turbomachinery*, Vol. 137, No. 2, Feb. 2015.
doi: 10.1115/1.4028235

[6] Borradile, J., "Towards the Optimum Ducted UHBR Engine," *24th Joint Propulsion Conference*, July 1988. doi: 10.2514/6.1988-2954

[7] Gunn, E. J., Brandvik, T., and Wilson, M. J., "Fan-Intake Coupling with Conventional and Short Intakes," *ASME Turbo Expo 2021: Volume 1, Aircraft Engine; Fans and Blowers; Marine; Wind Energy; Scholar Lecture*, Vol. 1, June 2021, pp. 1–12. doi: 10.1115/GT2021-58829

[8] Siervi, F. De, Viguier, H. C., Greitzer, E. M., and Tan, C. S., "Mechanisms of Inlet-Vortex Formation," *Journal of Fluid Mechanics*, Vol. 124, No. 1, 1982, pp. 173–193.
doi: 10.1017/S0022112082002456

[9] Shin, H. W., Greitzer, E. M., Cheng, W. K., Tan, C. S., and Shippee, C. L., "Circulation Measurements and Vortical Structure in an Inlet-Vortex Flow Field," Journal of Fluid Mechanics, Vol. 162, 1986, pp. 463–487.
doi: 10.1017/S0022112086002124

[10] Brix, S., Neuwerth, G., and Jacob, D., "The Inlet-Vortex System of Jet Engines Operating Near the Ground," 18th Applied Aerodynamics Conference, AIAA Paper 2000-3998, Denver, CO, 2000.
doi: 10.2514/6.2000-3998

[11] Liu, W., Greitzer, E. M., and Tan, C. S., "Surface Static Pressures in an Inlet Vortex Flow Field," Journal of Engineering for Gas Turbines and Power, Vol. 107, No. 2, Apr. 1985, pp. 387–393.
doi: 10.1115/1.3239738

[12] Nakayama, A., and Jones, J. R., "Correlation for Formation of Inlet Vortex," *AIAA Journal*, Vol. 37, No. 4, Apr. 1999, pp. 508–510.
doi: 10.2514/2.743

[13] Trapp, L. G., and da Motta Girardi, R., "Crosswind Effects on Engine Inlets: The Inlet Vortex," *Journal of Aircraft*, Vol. 47, No. 2, Mar. 2010, pp. 577–590.
doi: 10.2514/1.45743

[14] El-Sayed, A. F., and Emeara, M. S., "Aerodynamics of Intakes of High Bypass Ratio (HBPR) Turbofan Engines," *International Robotics and Automation Journal*, Vol. 6, No. 2, Jun. 2020, pp. 88–97.
doi: 10.15406/iratj.2020.06.00206

[15] Quémard, C., Garçon, F., and Raynal, J., "High Reynolds Number Air Intake Tests in the ONERA F1 and S1MA Wind Tunnels," *Workshop on Airframe Engine Integration*, DLR, Braunschweig, Germany, Mar. 1996.

[16] Lecordix, J., Mullender, A., Lecossais, E., Godard, J., and Hepperle, M., "Hybrid Laminar Flow Nacelle Design," *ICAS Proceedings*, Vol. 20, 1996, pp. 504–520.

[17] Colin, Y., Aupoix, B., Boussuge, J.-F., and Chanez, P., "Numerical Simulation and Analysis of Crosswind Inlet Flows at Low Mach Numbers," *8th International Symposium on Experimental and Computational Aerothermodynamics of Internal Flows*, Lyon, France, July 2007.

[18] Zhang, M., "Numerical Investigation of Nacelle Intake Flow Distortion at Crosswind Conditions," *32nd Congress of the International Council of the Aeronautical Sciences*, ICAS 2021, 2021, pp. 1–11.

[19] Harjes, L., Bode, C., Grubert, J., Frantzheld, P., Koch, P., and Friedrichs, J., "Investigation of Jet Engine Intake Distortions Caused by Crosswind Conditions," Journal of the Global Power and Propulsion Society, Vol. 4, May 2020, pp. 48–62.
doi: 10.33737/jgpps/118875

[20] Burnazzi, M., Probst, A., and Steger, M., "Hybrid RANS/LES of an Isolated Engine Nacelle with Crosswind Using an Unstructured CFD Solver," Progress in Hybrid RANS-LES Modelling, Vol. 143, 2020, pp. 347–356.
doi: 10.1007/978-3-030-27607-2_28

[21] Murphy, J. P., Taylor, M. D., and MacManus, D. G., "A Quantitative Study of Intake Ground Vortices," 18th International Symposium on Air Breathing Engines (ISABE), Beijing, China, 2007.

[22] Murphy, J. P., and MacManus, D. G., "Ground Vortex Aerodynamics under Crosswind Conditions," *Experiments in Fluids*, Vol. 50, No. 1, 2011, pp. 109–124.
doi: 10.1007/s00348-010-0902-4

[23] Zantopp, S., MacManus, D., and Murphy, J., "Computational and Experimental Study of Intake Ground Vortices," *The Aeronautical Journal*, Vol. 114, No. 1162, Dec. 2010, pp. 769–784.
doi: 10.1017/S0001924000004255

[24] Wang, Z., and Gursul, I., "Unsteady Characteristics of Inlet Vortices," Experiments in Fluids, Vol. 53, No. 4, Oct. 2012, pp. 1015–1032.
doi: 10.1007/s00348-012-1340-2
[25] Courtine, S., Bouchet, J.-P., Guibert, A., Gauducheau, B., Costa, R. M. e, and Raynal, S., "Experimental Characterization of Intake Ground Vortex Ingestion under Crosswind Conditions in Wind Tunnel," *56th 3AF International Conference on Applied Aerodynamics*, 2022.
[26] Nichols, D. A., Vukasinovic, B., Glezer, A., and Rafferty, B., "Formation of a Nacelle Inlet Ground Vortex in Crosswind," AIAA SciTech 2022 Forum, AIAA Paper 2022-1698, San Diego, CA, 2022.
doi: 10.2514/6.2022-1698
[27] Nichols, D. A., Vukasinovic, B., and Glezer, A., "Scaling Characteristics of Ground Vortices in a Nacelle Inlet Flow Field," AIAA SciTech 2023 Forum, AIAA Paper 2023-1981, National Harbor, MD, 2023.
doi: 10.2514/6.2023-1981
[28] Nichols, D. A., Vukasinovic, B., and Glezer, A., "The Formation, Evolution, and Sustainment of Inlet Ground Vortices," AIAA Aviation 2023 Forum, AIAA Paper 2023-3891, San Diego, CA, 2023.
doi: 10.2514/6.2023-3891
[29] Nichols, D. A., Vukasinovic, B., and Glezer, A., "Control of a Nacelle Inlet Ground Vortex," AIAA SciTech 2024 Forum, AIAA Paper 2024-2138, Orlando, FL, 2024.
doi: 10.2514/6.2024-2138
[30] Boscagli, L., Christie, R., MacManus, D., and Piovesan, T., "Aerodynamics of a Short Intake in Crosswind," *Aerospace Science and Technology*, Vol. 129, 2022, p. 107826.
doi: 10.1016/j.ast.2022.107826
[31] Freeman, C., and Rowe, A. L., "Intake Engine Interactions of a Modern Large Turbofan Engine," *ASME Turbo Expo*, 1999, pp. 3–8.
doi: 10.1115/99-GT-344
[32] di Mare, L., Simpson, G., and Sayma, A. I., "Fan Forced Response Due to Ground Vortex Ingestion," ASME Turbo Expo 2006: Power for Land, Sea, and Air, Paper GT2006-90685, Barcelona, Spain, 2006.
doi: 10.1115/GT2006-90685
[33] Green, J. S., "Forced Response of a Large Civil Fan Assembly," ASME Turbo Expo 2008: Power for Land, Sea, and Air, Paper GT2008-50319, Berlin, Germany, 2008.
doi: 10.1115/GT2008-50319
[34] Bissinger, N. C., and Breuer, T., "Basic Principles – Gas Turbine Compatibility – Intake Aerodynamic Aspects," *Encyclopedia of Aerospace Engineering*, Wiley, 2010, pp. 1–10.
[35] Doll, U., et al., "Non-Intrusive Flow Diagnostics for Unsteady Inlet Flow Distortion Measurements in Novel Aircraft Architectures," *Progress in Aerospace Sciences*, Vol. 130, Apr. 2022, p. 100810.
doi: 10.1016/j.paerosci.2022.100810
[36] Kompenhans, J., et al., "Particle Image Velocimetry in Aerodynamics: Technology and Applications in Wind Tunnels," *Journal of Visualization*, Vol. 2, Nos. 3–4, Sep. 2000, pp. 229–244.
doi: 10.1007/BF03181440
[37] Kempaiah, K. U., et al., "High-Resolution Turbofan Intake Flow Characterization by Automated Stereoscopic-PIV in an Industrial Wind Tunnel Environment," *Measurement Science and Technology*, Vol. 35, No. 2, Feb. 2024, p. 025210.
doi: 10.1088/1361-6501/ad0ea0
[38] Stuermer, A. W., and Geisler, R., "CFD Modeling of Turbofan Intake Aerodynamics at Crosswind Conditions," *AIAA AVIATION 2023 Forum*, 2023.
doi: 10.2514/6.2023-3306
[39] Piovesan, T., Zachos, P. K., MacManus, D. G., Kempaiah, K., Michaelis, D., van Rooijen, B., Vahdati, M., and Sheaf, C., "Coupled Fan–Intake Dynamic Distortion Characterization at Crosswind Conditions," *AIAA Journal*, Vol. 63, No. 2, 2025, pp. 811–815.
doi: 10.2514/1.J064595
[40] Vassberg, J., Dehaan, M., Rivers, M., and Wahls, R., "Development of a Common Research Model for Applied CFD Validation Studies," AIAA Paper 2008-6919, 26th AIAA Applied Aerodynamics Conference, 2008.
doi: 10.2514/6.2008-6919
[41] Seddon, J., and Goldsmith, E., *Intake Aerodynamics*, 2nd ed., AIAA, Washington, DC, 1999.
doi: 10.2514/4.473616
[42] SAE S-16 Committee, "Gas Turbine Engine Inlet Flow Distortion Guidelines," Society of Automotive Engineers, Tech. Rep. ARP1420C, 2017.
[43] Scarano, F., and Riethmuller, M. L., "Advances in Iterative Multigrid PIV Image Processing," Experiments in Fluids, Vol. 29, No. 7, Dec. 2000.
doi:10.1007/s003480070007.
[44] SAE Aerospace Information Report 5686, "A Methodology for Assessing Inlet Swirl Distortion," Society of Automotive Engineers, 2022.

[45] Piovesan, T., Zachos, P. K., MacManus, D. G., and Sheaf, C., "Unsteady Swirl Distortion in a Short Intake under Crosswind Conditions," *AIAA Journal*, Vol. 63, No. 5, 2025, pp. 1867–1884.
doi: 10.2514/1.J064226

[46] Gil-Prieto, D., Zachos, P., MacManus, D. G., and Tanguy, G., "Convoluted Intake Distortion Measurements Using Stereo Particle Image Velocimetry," *34th AIAA Applied Aerodynamics Conference*, Washington, DC, 2016.
doi: 10.2514/6.2016-3560

[47] Burcham, F. W. J., Hughes, D. L., and Holzman, J. K., "Steady-State and Dynamic Pressure Phenomena in the Propulsion System of an F-111A Airplane," NASA Technical Note NASA-TN-D-7328, 1973.

[48] Bowditch, D. N., and Coltrin, R. E., "A Survey of Inlet/Engine Distortion Compatibility," NASA TM-83421, 1983.

[49] SAE S-16 Committee, "Inlet Total-Pressure Distortion Considerations for Gas-Turbine Engines," Society of Automotive Engineers, Tech. Rep. AIR1419D, Revision D, Aug. 2023.
doi:10.4271/AIR1419D.

[50] Jacocks, J. L., and Kneile, K. R., "Statistical Prediction of Maximum Time-Variant Inlet Distortion Levels," AEDC Tech. Rep. AEDC-TR-74-121, 1975.

[51] Kidman, D. S., Brownlow, J. D., Binkley, B. A., and Morris, C. C., "Application of Extreme Value Statistics to Reduce Test and Computational Requirements for Quantifying Maximum Engine Inlet Total Pressure Distortion," *23rd International Symposium on Air Breathing Engines (ISABE)*, Manchester, UK, 2017.

[52] Jacocks, J., "Statistical Analysis of Distortion Factors," *8th Joint Propulsion Specialist Conference*, New Orleans, LA, 1972.
doi: 10.2514/6.1972-1100

[53] Gil-Prieto, D., MacManus, D. G., Zachos, P. K., and Bautista, A., "Assessment Methods for Unsteady Flow Distortion in Aero-Engine Intakes," *Aerospace Science and Technology*, Vol. 72, Jan. 2018, pp. 292–304.
doi: 10.1016/j.ast.2017.10.029

[54] Migliorini, M., Zachos, P. K., MacManus, D. G., and Haladuda, P., "S-Duct Flow Distortion with Non-Uniform Inlet Conditions," *Proceedings of the Institution of Mechanical Engineers, Part G: Journal of Aerospace Engineering*, Vol. 237, No. 2, 2023, pp. 357–373.
doi: 10.1177/09544100221101669

[55] Coles, S., *An Introduction to Statistical Modeling of Extreme Values*, Springer, 2001.

[56] Sarabia, J. M., Hadi, A. S., Castillo, E., and Balakrishnan, N., *Extreme Value and Related Models with Applications in Engineering and Science*, Wiley, 2004.

[57] Piovesan, T., Zachos, P. K., MacManus, D. G., Michaelis, D., van Rooijen, B., Sheaf, C., and Arzoglou, D., "Use of Non-Intrusive Flow Diagnostics for Aero-Engine Inlet Flow Distortion Measurements in an Industrial Wind Tunnel," *AIAA SCITECH 2025 Forum*, Jan. 2025, AIAA 2025-2111.

[58] Meyer, W., Pazur, W., and Fottner, L., "The Influence of Intake Swirl Distortion on the Steady-State Performance of a Low Bypass, Twin-Spool Engine," AGARD, Tech. Rep. AGARD-CP-498, 1991.

[59] Breuer, T., and Bissinger, N. C., "Basic Principles — Gas Turbine Compatibility — Gas Turbine Aspects," in Encyclopedia of Aerospace Engineering, Wiley, Dec. 2010, pp. 1–12.
doi: 10.1002/9780470686652.eae573



https://dspace.org/

Unsteady swirl distortion characterization in a coupled fan-intake system in crosswind conditions using stereoscopic particle image velocimetry

Piovesan, Tommaso; Zachos, Pavlos K.; MacManus, David G.

2026-01-16
American Institute of Aeronautics and Astronautics (AIAA)
https://doi.org/10.2514/6.2026-2569
Piovesan T, Zachos PK, MacManus D. (2026) Unsteady swirl distortion characterization in a coupled fan-intake system in crosswind conditions using stereoscopic particle image velocimetry. In: AIAA SCITECH 2026 Forum, 12-16 January 2026, Orlando, Florida, Article number 2026-2569

Downloaded from a DSpace repository. https://dspace.org/